


Article

Laser Pulse Effects on Plasma-Sprayed and Bulk Tungsten

Roberto Montanari *, Ekaterina Pakhomova, Roberto Pizzoferrato , Maria Richetta and Alessandra Varone

Department of Industrial Engineering, University of Rome Tor Vergata, 00133 Rome, Italy; pakhomovaea@mail.ru (E.P.); pizzoferrato@uniroma2.it (R.P.); richetta@uniroma2.it (M.R.); alessandra.varone@uniroma2.it (A.V.)

* Correspondence: roberto.montanari@uniroma2.it; Tel.: +39-6-7259-7197

Received: 9 October 2017; Accepted: 24 October 2017; Published: 26 October 2017

Abstract: Tungsten (W) is considered a promising plasma-facing material for protecting the divertor of the ITER (International Thermonuclear Experimental Reactor). The effects on W of transient thermal loads of high energy occurring in a tokamak under operative conditions have been simulated through a single laser pulse delivered by an Nd:YAG laser. Bulk and plasma-sprayed (PS) samples have been submitted to tests and successively examined via SEM (scanning electron microscopy) observations. In both types of materials, the laser pulse induces similar effects: (i) a crater forms in the spot central area; (ii) all around the area, the ejection and the movement of molten metal give rise to a ridge; (iii) in a more external area, the surface shows plates with jagged boundaries and cracks induced by thermal stresses; (iv) the pores present in the original material become preferred ablation sites. However, the affected surface area in PS samples is larger and asymmetric if compared to that of bulk material. Such a difference has been explained by considering how microstructural characteristics influence heat propagation from the irradiated spot, and it was found that grain size and shape play a decisive role.

Keywords: tungsten; plasma spraying; laser; microstructure; nuclear fusion reactors

1. Introduction

W has excellent thermo-mechanical properties, high thermal conductivity, low physical sputtering rate, low tritium inventory, and the highest melting point among all metals, so it is considered a promising plasma-facing material for the armors protecting the divertor of the ITER (International Thermonuclear Experimental Reactor) [1–6]. It has been already used in reactors like Joint European Torus (JET) [7] and Axially Symmetric Divertor Experiment Upgrade (ASDEX-U) [8] as a thin coating on substrates of carbon fiber composites (CFCs) and graphite.

Tiles of bulk tungsten (W) can be used to build up armors, but this approach presents certain drawbacks, namely the high brittle-to-ductile transition temperature (around 400 °C) and the intrinsic difficulties in machining. An alternative solution consists in coating the parts to protect with a W layer. Much work has been devoted to investigate suitable coating technologies and plasma spray (PS) in vacuum [2,9], physical vapor deposition (PVD) [10,11], and chemical vapor deposition (CVD) [12] have been proposed and tested under high heat flux loading. Yahiro et al. [13] investigated air plasma spray (APS) comparing the characteristics of coatings with those obtained through PS made in vacuum. In general, APS coatings present a higher content of oxygen and oxides, and porosity that worsens the thermo-mechanical properties [14–16].

A previous work of one of the present authors demonstrated the feasibility of depositing 5 mm thick W coatings on CuCrZr substrates by means of PS and their ability to withstand heat fluxes up

to $5 \text{ MW}\cdot\text{m}^{-2}$ in conditions relevant for fusion reactor plasma-facing components [2]. The specific coating characteristics, i.e., morphology, structure, integrity and mechanical properties, were then thoroughly investigated [17–19].

W is expected to resist to a steady state heat flux of $10 \text{ MW}\cdot\text{m}^{-2}$, and transient high energy events, such as disruption, edge localized modes, and vertical displacement events [6]. An aspect of fundamental importance is the interaction between W and plasma, which has been investigated either in fusion devices such as TEXTOR [20], ASDEX-U [21], and PF-1000 facility [22] or through laboratory simulations [23–32]. Particular attention has been paid to steady thermal loads, while some studies have focused on transient high heat loads, which may induce serious damage and degradation of W.

In this work, an Nd:YAG high power laser source was used to simulate the peculiar conditions described above, namely a high thermal load released in a very short time on a small surface area ($\sim 200 \mu\text{m}$) of PS and bulk W samples. The effects of the laser pulse have been examined by scanning electron microscopy (SEM) observations and discussed on the basis of the specific microstructural features of the two types of W considered in the experiments.

2. Materials and Experimental

2.1. Sample Characteristics

Two sets of samples have been examined: (i) plasma-sprayed W and (ii) bulk W supplied by PLANSEE (Metallwerk Plansee, Reutte, Austria).

The PS samples (Set 1) were prepared by depositing W on a substrate of the CuCrZr alloy. All the spraying campaigns were carried out in an argon atmosphere with a pressure of 600 mbar. The deposition parameters and the mechanical characteristics of the samples are shown in Tables 1 and 2, respectively. More details can be found in [33].

Table 1. Plasma-sprayed (PS) deposition parameters.

PS Deposition Parameters	
Plasma gas	Argon + Hydrogen
Plasma power	45 kW
Torch to substrate distance	180 mm
Torch speed	$800 \text{ mm}\cdot\text{s}^{-1}$
Spraying atmosphere	Argon
Deposition temperature	$<170 \text{ }^\circ\text{C}$

Table 2. Properties of PS and bulk tungsten (W).

Properties	PS W (Set 1)	Bulk W (Set 2)
Density ($\text{g}\cdot\text{cm}^{-3}$)	17.80	18.38
Mean grain size (μm)	6	65
Dislocation density ρ (cm^{-2})	2.0×10^9	1.5×10^{10}
Thermal expansion coefficient α (K^{-1})	5.5×10^{-6}	4.5×10^{-6}
Young's modulus E (Gpa)	82 ± 6	339 ± 10
Yield Stress σ_Y (MPa)	794	1190
Micro-hardness (HV)	300	478

Bulk W (Set 2) had a purity of 99.97% and a porosity of 5%. The microstructure and mechanical properties have been investigated in previous works [33,34]. Owing to the presence of impurities, the cell parameter ($a = 0.320 \text{ nm}$) determined by means of XRD is slightly higher than that reported in XRD data files (JCPDS-ICDD 4-806) for pure W [35]. The main properties are reported in Table 2.

The mean density of PS W (Set 1), measured by a water pycnometer, was $17.8 \text{ g}\cdot\text{cm}^{-3}$ and corresponds to about 92% of the theoretical bulk density: this value is slightly lower of that (95%) of

bulk W (Set 2). The Young's modulus of PS samples is about 82 GPa and is much lower than that of bulk W (~340 GPa). Such a low value cannot be explained by the amount of porosity. Figure 1 shows light microscopy (Union Optical Co., Ltd., Tokyo, Japan) images of both sets of samples.

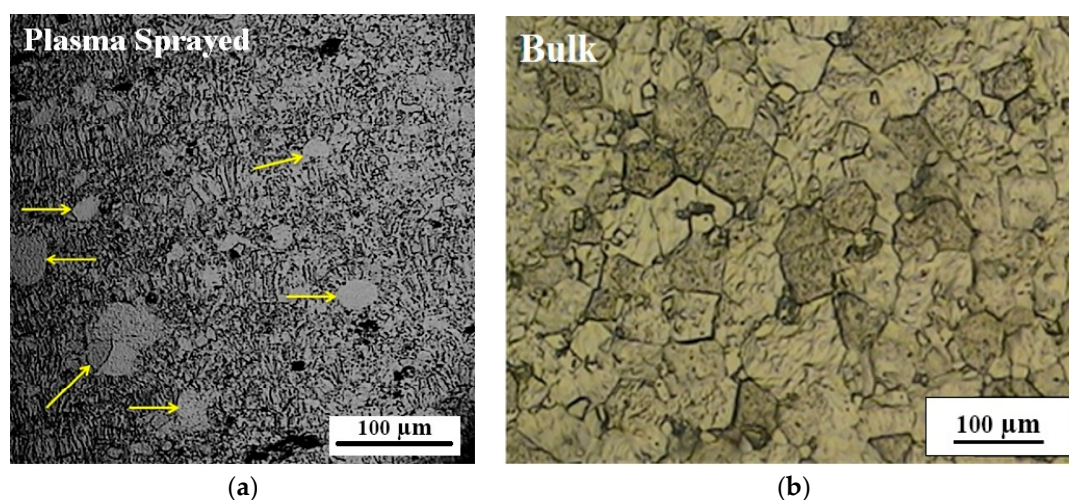


Figure 1. Structure the samples of Set 1 (a) and Set 2 (b).

PS samples exhibit a very fine layered structure. Moreover, some unmelted W particles (indicated by arrows) can be observed and represent points of mechanical weakness for the material. Even if plasma density is increased, for instance by slightly increasing the chamber pressure, or powders with finer granulometry and narrower size distribution are employed, the complete melting of W particles is a difficult task due to its refractory properties and high melting point.

Bulk W has a completely different structure consisting of nearly equiaxed grains (a mean size of 65 μm).

XRD (Philips, Eindhoven, The Netherlands) measurements have been carried out on both sets of samples by using Mo $K\alpha$ radiation ($\lambda = 0.071 \text{ nm}$). XRD spectra displayed in Figure 2 were recorded in a step scanning mode with 2θ steps of 0.05° and a counting time of 5 s per step. To investigate the crystalline texture, the relative intensities of the main reflections have been compared with those of W with random grain orientation, taken from the JCPDS-ICDD database [35]. The results, summarized in the table, show that PS and bulk W have textures similar to those of weak (100) and (211) components.

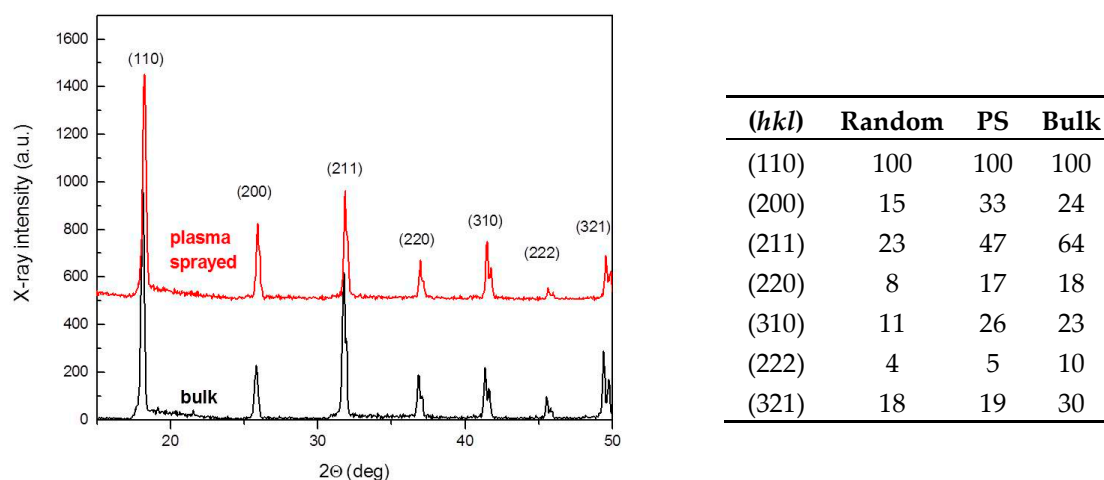


Figure 2. XRD spectra of bulk and plasma-sprayed W. The table summarizes the relative intensities of main reflections and compares these values with those of W with random oriented grains.

2.2. Laser Source

Transient thermal loads of high energy occurring in a tokamak under operative conditions have been simulated by the interaction with a single laser pulse delivered by the Nd:YAG laser TVLPS [30]. The source used in present experiments is a no-commercial laser composed by an Nd:YAG oscillator (QUANTEL SA, Orsay, France), based on Q-switched technique, followed by four amplification stages. The first two are also Nd:YAG, while the last ones are Nd:GLASS. The pulse parameters we used in the present experiments are as follows: wavelength $\lambda = 1064$ nm; pulse duration $\tau \approx 15$ ns; pulse energy $E_p \approx 8$ J; Transverse Electromagnetical Mode is TEM00; P-polarized; focal spot size $\Phi = 200$ μm ; surface power density on the focal plane $I = 1.7 \times 10^{12}$ $\text{W}\cdot\text{cm}^{-2}$. These parameters correspond to a plasma electronic temperature $T_e \approx 1.218 \times 10^6$ K at the critical surface [36] and allow for a simulation of the material degradation during the plasma disruption process.

The specific scope of the work was to investigate the effects of plasma-W interaction in a Tokamak, which operates in high vacuum conditions, so the samples were allocated in a vacuum chamber ($P \approx 10^{-5}$ bar).

Laser beam was focused on the target, mounted on a support with an incidence angle of 45° to minimize debris projection nearby target (see Figure 3).

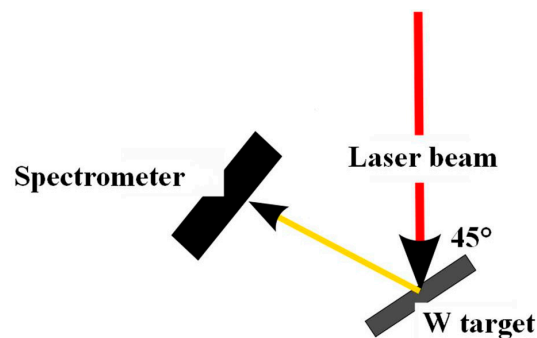


Figure 3. Experimental set-up.

Besides the energy loss in the optical path, the intensity of laser light is remarkably diminished by the reflection on the target, which is crucial to reach a desired surface temperature. The total reflectivity, namely, the sum of the specular reflectivity and diffuse reflectivity, has been determined for the W surface in an as-received condition and after mechanical polishing through a spectrophotometer (Lambda 950 from PerkinElmer, Waltham, MA, USA) in the wavelength range of 400–2400 nm. For the wavelength used in these experiments ($\lambda = 1064$ nm), the results in Figure 4 show reflectivities of about 60% and 48% in the cases of the polished and rough surfaces of the bulk sample, respectively.

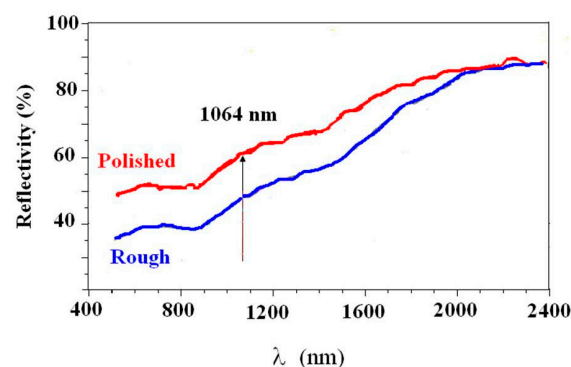


Figure 4. Total reflectivity vs. wavelength λ . The two curves refer to W with polished and rough surfaces.

After laser pulse exposure, the surface morphologies of PS and bulk samples have been characterized through SEM Hitachi SU70 (Hitachi, Tokyo, Japan) observations. Surface morphology of PS samples was also investigated through a 3D surface analyzer (TalySurf CLI 2000, Taylor Hobson, Leicester, UK) and TalyMap software Release 3.1 (Taylor Hobson, Leicester, UK).

3. Results and Discussion

Figure 5 displays SEM micrographs of bulk W taken in the zone irradiated by laser pulse. The main effect of the laser shot on bulk W is the formation of a crater with a conical shape, with a diameter of about 75 μm (Figure 5a,b), namely a little smaller than the laser spot, and a depth of about 25 μm . In this zone, the beam has the highest intensity and the major part of energy is released leading to material vaporization and melting. Laser pulse causes also the ejection of molten metal, which, after re-solidification during successive cooling, gives rise to the typical morphology with drops decorating the crater rim (Figure 5b). The Gaussian pulse shape implies that the intensity is maximum at the center and decreases towards the periphery with a temperature gradient, which leads to liquid movement along the radial direction, resulting in the formation of a ridge around the crater.

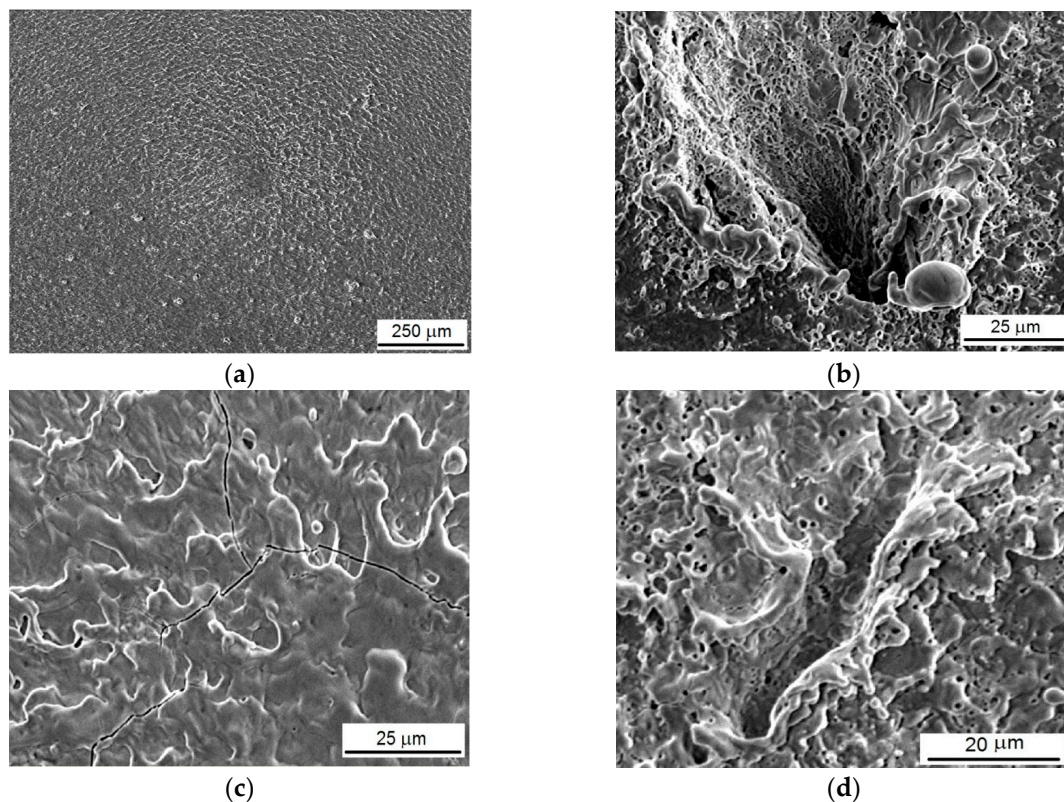


Figure 5. (a–d) Bulk W: SEM micrographs at different magnifications of the area irradiated by the laser pulse.

All around the crater an extended area shows a clear surface roughening (Figure 5c); the main feature consists of plates ranging from 10 μm to 30 μm with jagged boundaries, which arise from metal solidification. Thermal stresses due to fast heating and successive cooling produce an extended network of micro-cracks that often follow grain boundaries (Figure 5c). A similar network of micro-cracks was observed also by Chong et al. [25] in experiments carried out on W coatings realized through vacuum plasma spraying (VPS).

Furthermore, it is observed that the pores present in the material become preferred ablation sites. A previous work [32] evidenced that bulk W has a porosity of 5% consisting of very small

pores (~20 nm). In the area affected by laser pulse, the diameter of original pores increases by about one order of magnitude (see Figure 5d) confirming that low porosity is one of the most important requirements for W used as plasma-facing material.

The effects of laser pulse on PS material are shown in the SEM micrographs of Figure 6a–d. The area affected by laser pulse presents a roughly elliptical shape and is quite large (3 mm × 2 mm); inside this area, a crater with diameter of ~80 μm can be observed (Figure 6a,b). The mean level of the affected area, which is about 1–2 μm lower than that of the sample surface, testifies a loss of material. The crater depth is about 20 μm (Figure 6b). Therefore, laser pulse produces different damage in bulk and PS materials.

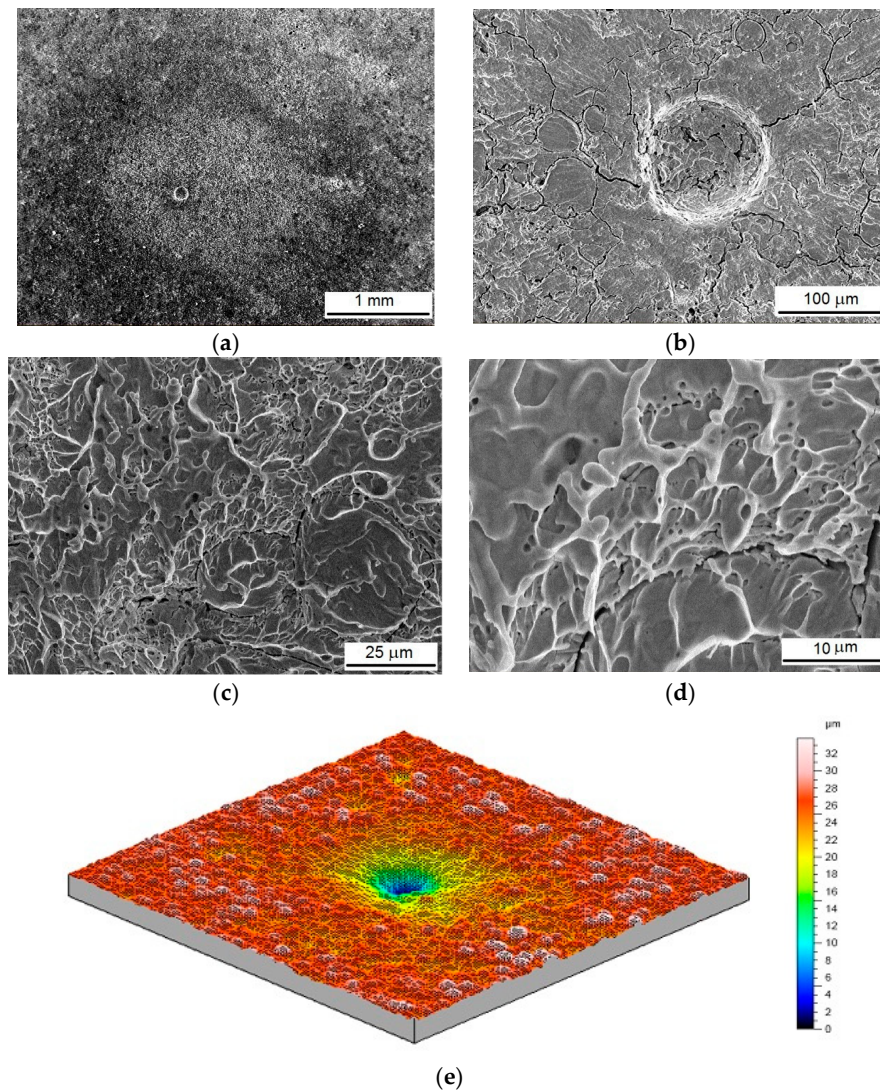


Figure 6. PS W: SEM micrographs at different magnification of the area irradiated by the laser pulse (a–d). Morphology of the same zone measured through the surface analyzer (e).

Surface roughening and micro-cracks occur also in PS W (Figure 6c), but the size of plates is smaller (about 5–6 μm) than that observed in the bulk material. The pore size is similar to that of bulk W (Figure 6d) and in the same way pores act as preferred ablation sites.

Figure 6e shows the morphology of the area affected by laser pulse achieved through a 3D surface analyzer; it is observed that the crater depth is about 20 μm.

From the comparison of Figures 5 and 6, it is clear that laser pulse produces different effects in bulk and plasma-sprayed W. Since the experimental conditions are the same the difference observed in

the two materials can be explained by considering a different propagation of heat from the irradiated spot. In the case of the PS material, the large and shallow affected area suggests that heat transfer occurs faster along the surface than in the direction perpendicular to the surface, whereas bulk W does not exhibit such anisotropic behavior. This can be ascribed to the different microstructure of PS and bulk materials examined in present experiments.

First of all, a possible effect of crystalline texture has been examined. When phonons travel through a single crystal their speed strongly depends on the specific lattice direction along which they move, so a preferred grain orientation in polycrystalline materials remarkably affects heat transfer (e.g., see [37]). However, XRD spectra in Figure 2 and the relative intensities of the most intense reflections (Table in Figure 2) indicate that PS and bulk W have similar textures, so this factor is not responsible for the observed different behavior of the two materials.

The density of grain boundaries, pores, and lattice defects acting as scattering centers for phonons is another important aspect that might play a relevant role in phonon motion and consequently in heat propagation. As shown in Table 2, the dislocation density ρ is one order of magnitude higher in bulk W ($\sim 10^{10} \text{ cm}^{-2}$) than in PS W ($\sim 10^9 \text{ cm}^{-2}$). In general, as the density of dislocations increases, thermal conductivity decreases; however, this factor does not affect the material isotropy. Analogous considerations can be made for the pores, which are a little denser in PS (relative density 0.92) than in bulk material (relative density 0.95). Therefore, the attention has been focused on grain boundaries.

Bulk W exhibits equiaxed grains of about $65 \mu\text{m}$, whereas PS W has a more complex and finer structure (see Figure 1). The PS microstructural features are clearly displayed in Figure 7a,b, showing a fracture surface obtained by breaking the coating through three points bending test.

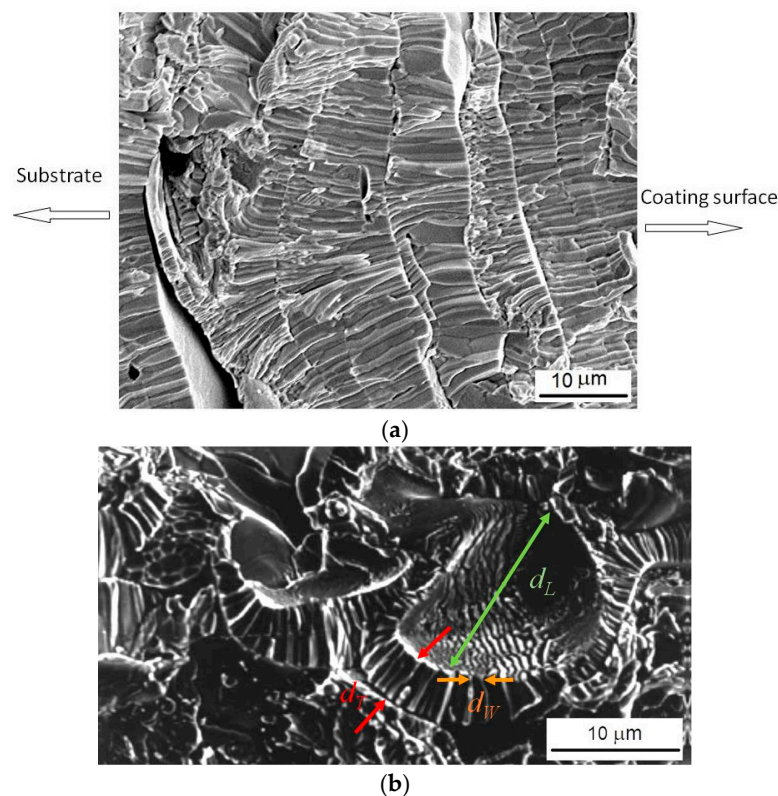


Figure 7. PS W: SEM micrographs of a fracture surface (a,b).

Figure 7a shows the layered structure originated by the splat of liquid W drops on the surface produced by the plasma spraying process. The layers are roughly parallel to the coating surface and have a thickness ranging from $2 \mu\text{m}$ to $4 \mu\text{m}$; for instance, the red arrows in Figure 7b indicate a layer

with thickness d_T of about 3 μm . In fact, interlayer surfaces represent a discontinuity for heat transfer. In addition, some cracks are observed.

Metal solidification gives rise to columnar grains inside each layer; their thickness is usually that of the layer, the width d_W is 1–2 μm , while the length d_L corresponds more or less to the size of the original splatted drop, namely some tens of microns. In fact, the grains exhibit an irregular lamella-like shape with one dimension much larger than the other two.

It is well known that thermal conductivity of crystalline materials is lower than that of the corresponding single crystal materials, and it decreases as grain sizes decrease; different theoretical models have been proposed, and a critical review can be found in [38]. Anyway, it is commonly assumed that the correlation between incoming and outgoing phonons is completely destroyed by the scattering occurring at an interface [39] (e.g., a grain boundary). The thermal conductivity C of a polycrystalline material can be written as:

$$C = \frac{C_0}{1 + \frac{C_0 R_K}{d}} \quad (1)$$

where d is the grain size, C_0 is the grain interior thermal conductivity, and R_K is the Kapitza resistance, which is a measure of an interface resistance to thermal flow [40,41]. The Kapitza resistance of W , usually expressed in $\text{K}\cdot\text{W}^{-1}\cdot\text{cm}^2$, depends on temperature T and can be represented for W by the Khalatnikov's power law [42]:

$$R_K = 2040T^{-3} \quad (2)$$

The value of C_0 at room temperature is $1.75 \text{ W}\cdot\text{cm}^{-1}\cdot\text{K}^{-1}$ and its temperature dependence obeys the empirical relationship [43]:

$$C_0 = 1.0834 - 1.052 \times 10^{-4}T + \frac{234.199}{T} \quad (3)$$

Figure 8 shows the thermal conductivity of W vs. temperature, calculated by introducing into Equation (1) the values of R_K and C_0 determined through Equations (2) and (3), respectively. Four cases are considered: (i) the bulk material with equiaxed grains ($d = 65 \mu\text{m}$); the PS material with $d_T = 3 \mu\text{m}$, $d_L = 25 \mu\text{m}$, and $d_W = 1 \mu\text{m}$. The values chosen for PS W are average values determined through several SEM observations. The comparison of the curves in Figure 8 allows a rough estimation of the thermal conductivity in both materials and in the three main directions of PS samples.

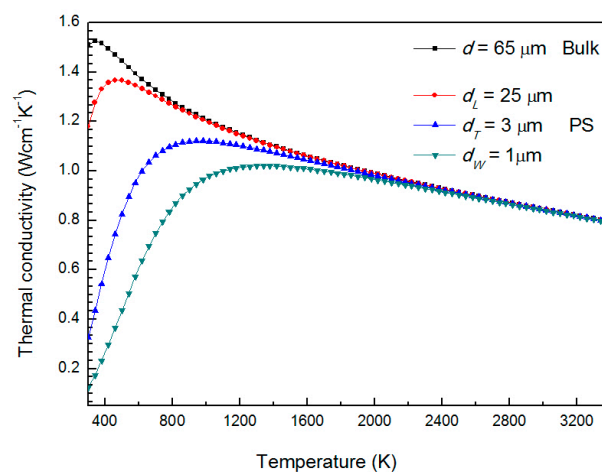


Figure 8. Thermal conductivity of W vs. temperature calculated for different grain sizes.

It can be observed that, above $\sim 2000 \text{ K}$, the effect of grain size on thermal conductivity can be considered negligible: the four curves are substantially overlapped. On the contrary, below $\sim 2000 \text{ K}$,

thermal conductivity remarkably depends on grain size and the curves tend progressively to diverge as temperature decreases. In conclusion, below 2000 K, heat transfer is different in bulk and PS materials, and for PS W it is different in the three main directions inside each solidified drop.

Heat transfer is an isotropic process in bulk W owing to its structure with equiaxed grains, whereas it is anisotropic in PS W. Each layer of PS material consists of many solidified drops formed by lamella-like grains, but the lattice orientation of adjacent solidified drops is not coherent, so their lamella-like grains are not aligned. In the case of a perfectly random distribution of the orientations, the anisotropic behavior typical of each drop will be cancelled, but PS material has two weak (100) and (211) texture components (see Figure 2), so the overall effect is not null and such anisotropy leads to the asymmetric shape of the affected zone. Another consequence is that heat travels easier along the surface than in the perpendicular direction, giving rise to a more extended affected area with respect bulk material. Of course, previous considerations regard the area where plates with jagged boundaries and cracks induced by thermal stresses are observed. The crater forms at a much higher temperature, far above the melting point, so there is no remarkable difference in size and shape in the two types of materials.

The crater depth is similar in bulk and PS W; the small observed difference is of the order of data scattering observed in experiments carried out on both materials. This depends on the very high temperature range where vaporization and melting, which produce the crater, occur. In fact, the microstructural features play a role during cooling below 2000 K (see Figure 8) when the crater has already formed and all of the material has solidified.

4. Conclusions

The effects on W of transient thermal loads of high energy occurring in a Tokamak under operative conditions have been simulated through a single laser pulse delivered by an Nd:YAG laser. Bulk and PS samples have been submitted to tests and successively examined via SEM observations.

In both types of materials, the laser pulse induces the same effects: (i) a crater forms in the spot central area; (ii) all around the area, the ejection and movement of molten metal gives rise to a ridge; (iii) in a more external area, the surface shows plates with jagged boundaries and cracks induced by thermal stresses; (iv) the pores present in the original material become preferred ablation sites. However, the affected surface area of PS W is larger and asymmetric if compared to that of bulk material. Such difference has been explained by considering how microstructural characteristics affect heat propagation from the irradiated spot. Porosity, texture, and dislocation density do not justify the morphology of affected surface areas, while grain size and shape seem to play a decisive role. Bulk W has equiaxed grains, so thermal conductivity is substantially the same in all the directions. On the contrary, the layered structure of PS material with lamella-like shaped grains gives rise to an anisotropic behavior; namely, thermal conductivity along the surface is higher than that in the perpendicular direction.

Author Contributions: All authors discussed and planned the experiments; Maria Richetta performed laser tests; Ekaterina Pakhomova and Alessandra Varone prepared the samples, carried out XRD measurements, and light microscopy observations; Roberto Pizzoferrato and Ekaterina Pakhomova made SEM observations; all authors contributed to the analysis of the results; Maria Richetta, Roberto Montanari, and Ekaterina Pakhomova wrote the manuscript.

Conflicts of Interest: The authors declare no conflict of interest.

References

1. Riccardi, B.; Pizzuto, A.; Bertamini, L.; Diotalevi, M.; Viedier, G. Development of tungsten coatings for ITER divertor components. In Proceedings of the 17th IEEE/NPSS Symposium on Fusion Engineering, San Diego, CA, USA, 6–10 October 1997; p. 910.
2. Riccardi, B.; Pizzuto, A.; Orsini, A.; Libera, S.; Visca, E.; Bertamini, L.; Casadei, F.; Severini, E.; Montanari, R.; Vesprini, R.; et al. Tungsten thick coatings for plasma facing components. *Fusion Technol.* **1998**, *31*, 223–226.

3. Roedig, M.; Kuehnlein, W.; Linke, J.; Merola, M.; Rigal, E.; Schedler, B.; Visca, E. Investigation of tungsten alloys as plasma facing materials for the ITER divertor. *Fusion Eng. Des.* **2002**, *61–62*, 135–140. [[CrossRef](#)]
4. Bolt, H.; Barabash, V.; Krauss, W.; Linke, J.; Neu, R.; Suzuki, S.; Nyoshida, N. Materials for the plasma-facing components of fusion reactors. *J. Nucl. Mater.* **2004**, *66–73*, 329–333. [[CrossRef](#)]
5. Lipa, M.; Durocher, A.; Tivey, R.; Huber, T.; Schedler, B.; Weigert, J. The use of copper alloy CuCrZr as a structural material for actively cooled plasma facing and in vessel components. *Fusion Eng. Des.* **2005**, *75–79*, 469–476. [[CrossRef](#)]
6. Uytendhouwen, I.; Decreton, M.; Hirai, T.; Linke, J.; Pintsuk, G.; Van Oost, G. Influence of recrystallization on thermal shock resistance of various tungsten grades. *J. Nucl. Mater.* **2007**, *363–365*, 1099–1103. [[CrossRef](#)]
7. Maier, H.; Hirai, T.; Rubel, M.; Neu, R.; Mertens, P.; Greuner, H.; Hopf, C.; Matthews, G.F.; Neubauer, O.; Piazza, G.; et al. Tungsten and beryllium armour development for the JET ITER-like wall project. *Nucl. Fusion* **2007**, *47*, 222. [[CrossRef](#)]
8. Herrmann, A.; Greuner, H.; Fuchs, J.C.; de Marné, P.; Neu, R. Experiences with tungsten coatings in high heat flux tests and under plasma load in ASDEX Upgrade. *Phys. Scr.* **2009**, *2009*, 014059. [[CrossRef](#)]
9. Deschka, S.; Garcia-Rosales, C.; Hohenauer, W.; Duwe, R.; Gauthier, E.; Linke, J.; Lochter, M.; Mallener, W.; Plochl, L.; Rodhammer, P.; et al. Manufacturing and high heat flux loading of tungsten coatings on fine grain graphite for the ASDEX-upgrade divertor. *J. Nucl. Mater.* **1996**, *233–237*, 645–649. [[CrossRef](#)]
10. Maier, H. Tungsten erosion in the baffle and outboard regions of the ITER-like ASDEX Upgrade divertor. *J. Nucl. Mater.* **2004**, *335*, 515–519. [[CrossRef](#)]
11. Maier, H.; Neu, R.; Greuner, H.; Hopf, C.; Matthews, G.F.; Piazza, G.; Hirai, T.; Counsell, G.; Courtois, X.; Mitteau, R.; et al. Tungsten coatings for the JET ITER-like wall project. *J. Nucl. Mater.* **2007**, *363–365*, 1246–1250. [[CrossRef](#)]
12. Hirai, T.; Kreter, A.; Linke, J.; Malzbender, J.; Ohgo, T.; Philipps, V.; Pintsuk, G.; Pospieszczyk, A.; Sakawa, Y.; Sergienko, G. Critical heat flux loading experiments on CVD-W coating in the TEXTOR tokamak. *Fusion Eng. Des.* **2006**, *81*, 175–180. [[CrossRef](#)]
13. Yahiro, Y.; Mitsuhashi, M.; Tokunaga, K.; Yoshida, N.; Hirai, T.; Ezato, K.; Suzuki, S.; Akiba, M.; Nakashima, H. Characterization of thick plasma spray tungsten coating on ferritic/martensitic steel F82H for high heat flux armor. *J. Nucl. Mater.* **2009**, *386–388*, 784–788. [[CrossRef](#)]
14. Hu, D.; Zheng, X.; Niu, Y.; Ji, H.; Chong, F.; Chen, J. Effect of oxidation behavior on the mechanical and thermal properties of plasma sprayed tungsten coatings. *J. Therm. Spray Technol.* **2008**, *17*, 377–384. [[CrossRef](#)]
15. Huang, J.J.; Li, X.J.; Chen, J.; Liu, Y.; Qi, B.; Jiang, S.S.; Wang, X.S.; Luo, G.N. Vacuum annealing enhances the properties of a tungsten coating deposited on copper by atmospheric plasma spray. *J. Nucl. Mater.* **2013**, *432*, 16–19.
16. Park, J.Y.; Yang, S.J.; Jin, Y.G.; Chong, R.P.; Kim, G.H.; Han, H.N. Effect of annealing with pressure on tungsten film properties fabricated by atmospheric plasma spray. *Met. Mater. Int.* **2014**, *20*, 1037–1042. [[CrossRef](#)]
17. Montanari, R.; Riccardi, B.; Volterri, R.; Bertamini, L. Characterisation of plasma sprayed W-coatings on a CuCrZr alloy for nuclear fusion reactor applications. *Mater. Lett.* **2002**, *52*, 100–105. [[CrossRef](#)]
18. Riccardi, B.; Montanari, R.; Casadei, M.; Costanza, G.; Filacchioni, G.; Moriani, A. Optimisation and characterisation of tungsten thick coatings on copper based alloy substrates. *J. Nucl. Mater.* **2006**, *352*, 29–35. [[CrossRef](#)]
19. Kaciulis, S.; Mezzi, A.; Montanari, R.; Ucciardello, N.; Volterri, R. Composition of plasma-sprayed tungsten coatings on CuCrZr alloy. *Surf. Interface Anal.* **2010**, *42*, 1197–1200. [[CrossRef](#)]
20. Tanabe, T.; Wada, M.; Ohgo, T.; Philipps, V.; Rubel, M.; Huber, A.; Von Seggern, J.; Ohya, K.; Pospieszczyk, A.; Schweer, B. Application of tungsten for plasma limiters in TEXTOR. *J. Nucl. Mater.* **2000**, *283–287*, 1128–1133. [[CrossRef](#)]
21. Krieger, K.; Maier, H.; Neu, R. Conclusions about the use of tungsten in the divertor of ASDEX Upgrade. *J. Nucl. Mater.* **1999**, *266–269*, 207–216. [[CrossRef](#)]
22. Kubkowska, M.; Skladnik-Sadowska, E.; Kwiatkowski, R.; Malinowski, K.; Kowalska-Strzeciwiłk, E.; Paduch, M.; Sadowski, M.J.; Pisarczyk, T.; Chodukowski, T.; Kalinowska, Z.; et al. Investigation of interactions of intense plasma streams with tungsten and carbon fibre composite targets in the PF-1000 facility. *Phys. Scr.* **2014**, *2014*, 014038. [[CrossRef](#)]

23. Ouaras, K.; Colina Delacqua, L.; Quirós, C.; Lombardi, G.; Redolfi, M.; Vrel, D.; Hassouni, K.; Bonnin, X. Experimental studies of the interactions between a hydrogen plasma and a carbon or tungsten wall. *J. Phys. Conf. Ser.* **2015**, *59*, 012029. [CrossRef]
24. Merola, M.; Bobin-Vastra, I.; Cardella, A.; Febvre, M.; Giancarli, L.; Salavy, J.F.; Salito, A.; Schedler, B.; Vieider, G. Manufacturing of a full scale baffle prototype for ITER with a CFC and W plasma spray armour. *Fusion Eng. Des.* **2000**, *49–50*, 289–294. [CrossRef]
25. Chong, F.L.; Chen, J.L.; Li, J.G.; Zheng, X.B. Failure behaviors of vacuum plasma sprayed tungsten coatings for plasma facing application. *J. Nucl. Mater.* **2009**, *386–388*, 780–783. [CrossRef]
26. Sadowskia, M.J.; Skladnik-Sadowskaa, E.; Malinowska, K.; Wołowski, J.; Marchenkoc, A.K.; Tsarenkoc, A.V. Investigation of laser interaction with tungsten target by means of time-resolved optical spectroscopy. *Radiat. Eff. Defects Solids* **2008**, *163*, 569–577. [CrossRef]
27. Linke, J.; Loewenhoff, T.; Massaut, V.; Pintsuk, G.; Ritz, G.; Rodig, M.; Schmidt, A.; Thomser, C.; Uytendhouwen, I.; Vasechko, V.; et al. Performance of different tungsten grades under transient thermal loads. *Nucl. Fusion* **2011**, *51*, 073017. [CrossRef]
28. Kurehashi, H.; Ohtsuka, Y.; Ueda, Y.; Kurishita, H. Effects of repeated short heat pulses on tungsten. *J. Nucl. Mater.* **2011**, *417*, 487–490. [CrossRef]
29. Zhou, Z.J.; Song, S.X.; Du, J.; Ge, C.C. High heat flux testing of tungsten plasma facing materials. *J. Nucl. Mater.* **2007**, *367–370*, 1468–1471. [CrossRef]
30. Farid, N.; Harilal, S.S.; El-Atwani, O.; Ding, H.; Hassanein, A. Experimental simulation of materials degradation of plasma-facing components using lasers. *Nucl. Fusion* **2014**, *54*, 012002. [CrossRef]
31. Huber, A.; Arakcheev, A.; Sergienko, G.; Steudel, I.; Wirtz, M.; Burdakov, A.V.; Coenen, J.W.; Kreter, A.; Linke, J.; Mertens, P.; et al. Investigation of the impact of transient heat loads applied by laser irradiation on ITER-grade tungsten. *Phys. Scr.* **2014**, *2014*, 014005. [CrossRef]
32. Richetta, M.; Gaudio, P.; Montanari, R.; Pakhomova, E.; Antonelli, L. Laser pulse simulation of high energy transient thermal loads on bulk and plasma sprayed W for NFR. *Mater. Sci. Forum* **2017**, *879*, 1576–1581. [CrossRef]
33. Deodati, P.; Donnini, R.; Montanari, R.; Ucciardello, N. Microstructural investigation on tungsten for applications in future nuclear fusion reactors. *Mater. Sci. Forum* **2012**, *706–709*, 835–840. [CrossRef]
34. Ciambella, L.; Donnini, R.; Montanari, R. Effects of heat treatments on tungsten for armours in NFR. *Mater. Sci. Forum* **2014**, *783–786*, 2353–2358. [CrossRef]
35. JCPDS-International Centre for Diffraction Data. Available online: <http://www.icdd.com/> (accessed on 9 October 2017).
36. Francucci, M.; Gaudio, P.; Martellucci, S.; Richetta, M. Spectroscopy methods and applications of the Tor Vergata laser-plasma facility driven by GW-level laser system. *Int. J. Spectrosc.* **2011**, *2011*, 792131. [CrossRef]
37. Bocchini, G.F.; Bovesecchi, G.; Coppa, P.; Corasaniti, S.; Montanari, R.; Varone, A. Thermal diffusivity of sintered steels with flash method at ambient temperature. *Int. J. Thermophys.* **2016**, *37*, 38. [CrossRef]
38. Dong, H.; Wen, B.; Melnik, R. Relative importance of grain boundaries and size effects in thermal conductivity of nanocrystalline materials. *Sci. Rep.* **2014**, *4*, 7037. [CrossRef] [PubMed]
39. Swartz, E.T.; Pohl, R.O. Thermal boundary resistance. *Rev. Mod. Phys.* **1989**, *61*, 605. [CrossRef]
40. Nan, C.-W.; Birringer, R.; Clarke, D.R.; Gleiter, H. Effective thermal conductivity of particulate composites with interfacial thermal resistance. *J. Appl. Phys.* **1997**, *81*, 6692–6699. [CrossRef]
41. Yang, H.-S.; Bai, G.-R.; Thompson, L.; Eastman, J. Interfacial thermal resistance in nanocrystalline yttria-stabilized zirconia. *Acta Mater.* **2002**, *50*, 2309–2317. [CrossRef]
42. Johnson, R.C.; Little, W.A. Experiments on the Kapitza resistance. *Phys. Rev.* **1963**, *130*, 596–604. [CrossRef]
43. Lassner, E.; Schubert, W.-D. *Tungsten Properties, Chemistry, Technology of the Element, Alloys, and Chemical Compounds*; Springer: New York, NY, USA, 1999.

